ADVANCED ENERGY MATERIALS
www.advenergymat.de

Understanding the Role of Cesium on Chemical Complexity in Methylammonium-Free Metal Halide Perovskites

Jonghee Yang, Diana K. LaFollette, Benjamin J. Lawrie, Anton V. Ievlev, Yongtao Liu, Kyle P. Kelley, Sergei V. Kalinin, Juan-Pablo Correa-Baena, and Mahshid Ahmadi**

Mixed cesium- and formamidinium-based metal halide perovskites (MHPs) are emerging as ideal photovoltaic materials due to their promising performance and improved stability. While theoretical predictions suggest that a larger composition ratio of Cs (≈30%) aids the formation of a pure photoactive α-phase, high photovoltaic performances can only be realized in MHPs with moderate Cs ratios. In fact, elemental mixing in a solution can result in chemical complexities with non-equilibrium phases, causing chemical inhomogeneities localized in the MHPs that are not traceable with global device-level measurements. Thus, the chemical origin of the complexities and understanding of their effect on stability and functionality remain elusive. Herein, through spatially resolved analyses, the fate of local chemical structures, particularly the evolution pathway of non-equilibrium phases and the resulting local inhomogeneities in MHPs is comprehensively explored. It is shown that Cs-rich MHPs have substantial local inhomogeneities at the initial crystallization step, which do not fully convert to the α-phase and thereby compromise the optoelectronic performance of the materials. These fundamental observations allow the authors to draw a complete chemical landscape of MHPs including nanoscale chemical mechanisms, providing indispensable insights into the realization of a functional materials platform.

1. Introduction

In recent decades, metal halide perovskites (MHPs) have attracted massive interest because of their excellent optoelectronic properties and ease of manufacturing, with tremendous photovoltaic (PV) performance of 25.8% (31.3% for tandem PV) observed in solution-processed devices.[1–5] The outstanding functionality observed in leading MHPs highlights an exciting path toward the commercialization of MHP PVs. A key factor constraining the realization of MHP PV technologies is the notorious thermodynamic instability of the photoactive α-phase. In particular, the α-phase formamidinium (FA) MHPs, which are the leading composition exhibiting excellent PV performances,[2–4] suffer from a thermodynamic instability and subsequent transformation to a hexagonal δ-phase under ambient conditions.[6,7]

It has been proposed that this instability can be alleviated by incorporating other monovalent cations – such as methylammonium (MA) or cesium – into the matrix to form alloy-like structures that mediate the tolerance factor of the lattice and promote entropy-driven thermodynamic stabilization.[8–11] Also, it has been found that the nanoscale inhomogeneities present in the mixed MHP system can improve carrier transport and thereby device performance.[12,13] However, the evaporation of volatile MA is known to destabilize films, so recent efforts have explored the potential for stability enhancement in CsFA mixed-cation systems where the non-volatile inorganic Cs provide more robust stabilization.[14–18]

Despite recent progress, it has been reported that the incorporation of inorganic components, typically alkali metal (i.e., potassium, rubidium, and Cs) halides, can leave clustered crystallites in the MHP matrix; the extent of such inhomogeneities increases with increasing concentration of the inorganic halides in the precursor solution.[19] Such inorganic crystallites are known to detrimentally affect the optoelectronic performance of the MHP matrix by impeding electrical transport and promoting recombination loss.[19,20]

The appearance of these secondary phases and the consequent local inhomogeneities in CsFA MHP films may be attributed to the low solubility of the inorganic precursors in solvents;

J. Yang, S. V. Kalinin, M. Ahmadi
Institute for Advanced Materials and Manufacturing
Department of Materials Science and Engineering
University of Tennessee
Knoxville, TN 37996, USA
E-mail: mahmadi3@utk.edu

D. K. LaFollette, J.-P. Correa-Baena
School of Materials Science and Engineering
Georgia Institute of Technology
Atlanta, GA 30332, USA
E-mail: jpcorrea@gatech.edu

B. J. Lawrie, A. V. Ievlev, Y. Liu, K. P. Kelley
The Center for Nanophase Materials Sciences
Oak Ridge National Laboratory
Oak Ridge, TN 37831, USA

B. J. Lawrie
Materials Science and Technology Division
Oak Ridge National Laboratory
Oak Ridge, TN 37831, USA

The ORCID identification number(s) for the author(s) of this article can be found under https://doi.org/10.1002/aenm.202202880.

DOI: 10.1002/aenm.202202880

the solvated inorganics and/or undissolved micro-crystallites can be readily precipitated upon solution processing.[21,22] The formation of local non-perovskite crystallites inevitably takes up partial cations and halides that were originally intended to be part of a homogenized phase.[23,24] This may distort the real stoichiometry of the initial photoactive α-CsFA MHP lattice, limiting the successful formation of a homogenized α-MHP with the desired composition and optoelectronic performance.[25] Moreover, it has been found that these non-perovskite phases can initialize nanoscale local degradation of the mixed cation MHP system.[20] Understanding the essence of these secondary phases – especially their fate of formation – can provide invaluable insights into the development of state-of-the-art MA-free MHP systems.

Because of the chemical complexity and sensitive nature of these systems, the formation of the nanoscopic local disorder can be readily initiated by subtle changes in chemical composition and processing conditions that can then evolve in multimodal ways. Probing these changes requires a state-of-the-art analytical tool capable of capturing the nanoscopic chemistry in MHPs. Time-of-flight secondary ion mass spectrometry (ToF-SIMS) has been used to provide spatially resolved chemical insights in the MHP system.[26–29] Meanwhile, hyperspectral cathodoluminescence (CL) microscopy techniques can spatially map the energetics of electronic transitions in MHPs.[13,20,30] Combined, these tools can provide a comprehensive, spatially resolved understanding of the nanoscopic chemistry and optoelectronic properties in MHPs.

Here, we systematically explore the influence of the Cs composition ratio on the phase evolution of CsFA MHP systems by identifying the crystal structure of resulting films with nanoscale spatial resolution. Two different Cs stoichiometries (33% and 17%; denoted as Cs-rich and Cs-moderate MHPs, respectively) were selected as model compositions of the CsFA MHPs. High-throughput exploration suggested Cs-moderate MHP as an optimal composition for high PV performance.[21,31] Meanwhile, theoretical predictions suggest that ≈30% Cs content could thermodynamically minimize the formation of both δ-$CsPbI_3$ and δ-$FAPbI_3$ phases (from α-MHP phase), which would help obtain a phase-stable and homogeneous MHP.[16] Informed by complementary ToF-SIMS and CL microscopies, the following key observations are revealed here: 1) considerable amounts of non-perovskite phases (i.e., CsI, δ-$CsPbI_3$, and δ-$FAPbI_3$) are present in the Cs-rich MHP before annealing. 2) These non-perovskite phases in Cs-rich MHPs are not completely converted after annealing at appropriate temperatures, whereas a nearly pure, homogeneous α-CsFA phase is formed in Cs-moderate MHP. 3) Meanwhile, excessive annealing temperatures again promote the formation of δ-phases and PbI_2 in both MHP systems, rather than eliminating them. 4) Additionally, the incorporation of Br (17%) can alleviate the formation of local phase inhomogeneities at the initial stage of MHP crystallization. Local analyses of the electrical properties using conductive atomic force microscopy (cAFM) and Kelvin probe force microscopy (KPFM) confirm that such non-perovskite phases, which act as electrical insulators, not only disrupt local conductivity by blocking current flow but also drastically compromise the MHP photocurrents/photovoltages. These observations describe the essential reasons why the performance and longevity of Cs-rich MHP PVs are inferior to those of their Cs-moderate counterparts.[32] Together, these measurements of spatially resolved physical/chemical landscapes provide a fundamentally new understanding of functional semiconducting materials and an ideal pathway to realize high-performance, long-lasting, mass-producible, and commercially viable MHP optoelectronics.

2. Results and Discussion

The desired long-term stability and optoelectronic performance of CsFA-based MHPs stem from the improved durability of the photoactive α-phase that results from the thermodynamic preference for the metastable structure.[11] However, high-throughput compositional exploration of these MHP systems revealed that there are still noticeable structural inhomogeneities including secondary phases and different grain sizes.[31] As these systems are made under relatively low temperatures, mixing such a multitude of chemical species could result in highly non-equilibrium phases associated with the crystallizing behaviors of each chemical species. Nevertheless, only the final structures of the MHP systems have been considered and investigated so far, particularly using device-level measurements. Such global measurements only provide bulk-averaged information, and thus, they cannot trace the chemical complexities of the MHP systems as well as the consequent effect of their functionalities, which remain uncovered.

Spatially resolved ToF-SIMS measurements were used to probe local inhomogeneities in the MHP film surfaces and their evolution with temperature.[26–28] For the pristine films before annealing, the ToF-SIMS positive ion maps revealed that Cs^+ (red) and FA^+ (green) cations are not homogeneously distributed over the analyzed areas (**Figure 1**a). Needle-like Cs aggregates – with respective lengths and widths of ≈10–20 and 1–2 µm – were prevalent over the surface of the Cs-rich ($x = 0.33$) MHP matrix. The local positions of Cs^+ are exclusively matched with those of I^-, Cs_2I^+, and CsI_2^-, as observed from the individual ion maps (Figures S1—S4, Supporting Information). Due to the very strong Cs^- and I^- signals,[33] the Pb^+ intensity at these aggregates is not appreciable, and it is difficult to assign these CsI-based aggregates to the δ-$CsPbI_3$ phase. However, these observations suggest that there are substantial phase inhomogeneities in the MHP films before annealing that are associated with the inorganic salt, CsI. Given the poor solubility of CsI in the solvents used here, these inorganic salts might be precipitated out, or undissolved micro-crystallites might be left after solution processing, in accordance with a previous report.[21,31]

Interestingly, the distinctive CsI-based aggregates undergo notable phase transformations during thermal annealing. After annealing at 150 °C, the needle-structured CsI-based aggregates start to melt/disappear (Figure 1b) and both Cs^+ and FA^+ (as well as I^-, as shown in Figure S1, Supporting Information) appear more homogenous across the MHP film. Note that the Cs-rich MHPs still exhibit CsI-based aggregated regions, whereas the Cs^+ and FA^+ cations in the Cs-moderate MHP are spatially homogenized. These observations indicate that annealing at 150 °C converts the aggregates to MHP phases

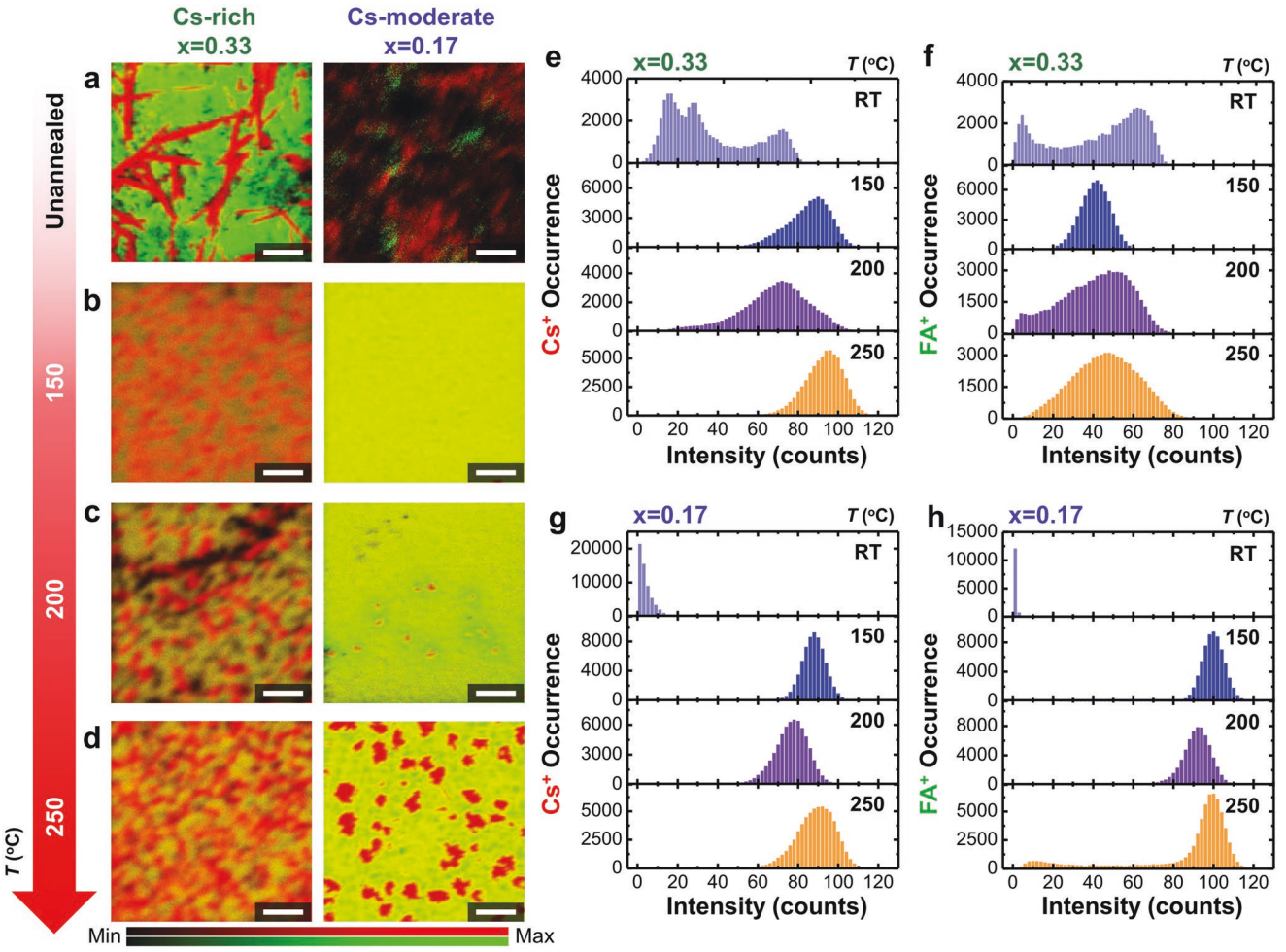

Figure 1. a–d) Overlays of Cs^+ (red) and FA^+ (green) maps by ToF-SIMS spectrometry of $Cs_xFA_{1-x}PbI_3$ MHP systems with increasing annealing temperature (Scale bar: 5 µm). Statistical histograms of e,g) Cs^+ and f,h) FA^+ ion intensities estimated from the corresponding ToF-SIMS maps: e,f) Cs-rich and g,h) Cs-moderate MHPs, respectively.

and eliminates the local inhomogeneities in the Cs-moderate film, suggesting that the applied thermal energy is sufficient to overcome the thermodynamic barrier for the transformation of non-perovskite phases to the photoactive α-phase.[31] In contrast, the significant compositional disorder in Cs-rich MHP (i.e., CsI-based aggregates) cannot be fully mediated by annealing at 150 °C, even though relatively lower temperatures < 100 °C are required for the δ-to-α phase transition in $Cs_{0.3}FA_{0.7}$ MHPs.[16]

The chemical disorder in the Cs-rich MHPs was not alleviated after annealing the films at 200 °C (Figure 1c). This indicates that the formation of homogeneous Cs-rich α-MHPs is not feasible by just controlling temperature, and control of solvents, additives, etc. is likely needed to improve the film homogeneity. Additionally, the homogeneous Cs-moderate MHP annealed at 150 °C exhibits increased heterogeneity at an annealing temperature of 200 °C: CsI-based aggregates emerge due to the deformation of the α-CsFA MHP phase. For films annealed at 250 °C, the number and size of CsI-based aggregates increase further in all films (Figure 1d). This implies that the deformation of MHPs might result from the thermal decomposition of FA^+,[34] suggesting that annealing temperatures > 200 °C are inappropriate for functional MHP films.

The histograms of ToF-SIMS intensities in Figure 1e–h illustrate qualitative changes of each ion in the MHP film as a function of annealing temperature. While the Cs-rich iodide MHP exhibits broader and disordered features, the Cs^+ and FA^+ distributions narrow after annealing at 150 °C (Figure 1e,f). This indicates that moderate heat induces a phase transformation process that results in a relatively homogeneous ion distribution over the MHP matrices. The spatially homogenized chemical compositions are particularly clear in the Cs-moderate MHP. The Cs^+ distributions become broader and shift towards higher intensity levels as the annealing temperature increases to 250 °C as a result of Cs aggregation which is also observed in the corresponding ion maps. Similar trends were observed for I^- (Figure S5, Supporting Information). This suggests that, at excessive temperatures, phase transformation processes are mainly associated with Cs^+, but nontrivial reaction pathways of I^- with other cations (e.g., Pb^+) are also present. In contrast, the distributions of FA^+ – though they also become broader – shift towards low-intensity levels, resulting in lower FA^+ to

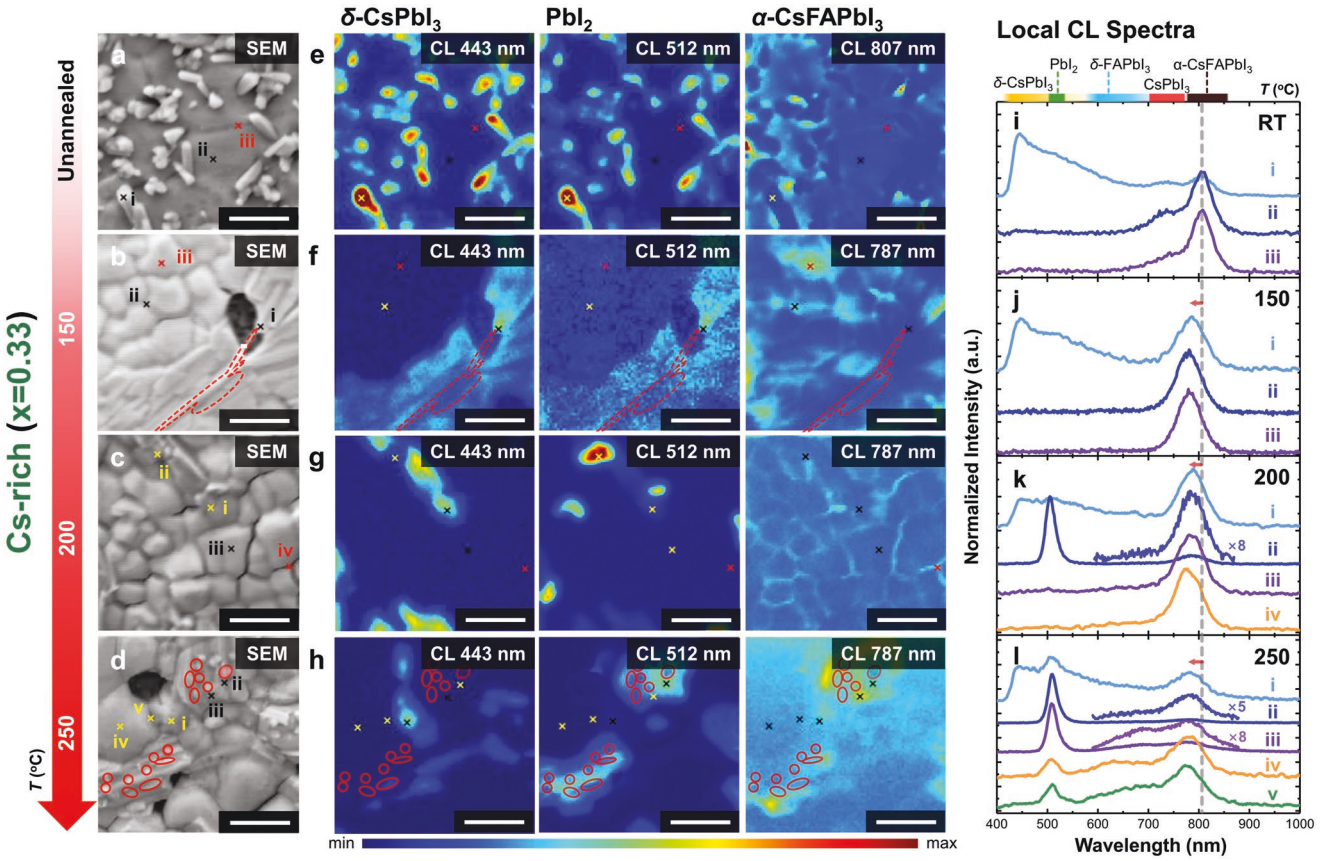

Figure 2. a–d) SEM images, e–h) CL microscopy maps, and i–l) local CL spectra (from positions marked in SEM image) of Cs-rich iodide MHPs, with increasing annealing temperature: a,e,i) unannealed, b,f,j) annealed at 150 °C, c,g,k) annealed at 200 °C, and d,h,l) annealed at 250 °C, respectively. Scale bar: 1 µm. The regions highlighted with red lines indicate the Cs-inactive area, assigned to be CsI. For i–l), the spectral regions where the CL peak corresponds to each phase are displayed as a color bar on top of the plot. In (e) and (f), the similarity in 443 and 512 nm-passed CL maps is due to the broadband δ-$CsPbI_3$ CL emission and the absence of PbI_2 CL.

Cs^+ intensity ratios (Figure S6, Supporting Information). This may be ascribed to the evaporation of FA^+ during annealing at higher temperatures, as previously reported for pure $FAPbI_3$ MHPs.[34]

Upon Br incorporation, the sizes of CsI-based aggregates become smaller and the Br-related signals are strongly spatially correlated with the CsI-based aggregates (Figures S3, S4, and S7, Supporting Information). These features might be due to a chemical equilibrium in the halide exchange reaction of CsI (with Br) driven by the existence of free Br^- ions (that result from the dissolution of FABr) in the precursor solution (Note S1, Supporting Information).[35,36] In addition, relative drops of Br ion intensity were observed in the mixed-halide system annealed at 250 °C (Figures S8 and S9, Supporting Information), as a result of Br evaporation at the film surface (Note S1, Supporting Information).[34]

Overall, ToF-SIMS observations clearly reveal the presence of substantial CsI-based aggregates in the MHP thin films before annealing. However, we could not precisely assign these to CsI or δ-$CsPbI_3$ at this stage as the intensities of Cs^+ and I^- ion mass are too strong; these elements are readily ionized during measurement and the intensity of Pb^+ ion mass observed at these regions are relatively weak. By thermal annealing at 150 °C, these inorganic aggregates in Cs-moderate MHP are homogenized into the films to form the α-CsFA MHP phase, whereas those in Cs-rich MHP partially remain in the film and couldn't fully transform to the desired phase. In both cases, further raising the annealing temperature produces additional CsI-based aggregates on the MHP surface by decomposition of FA^+.

Hyperspectral imaging of the CsFA MHP films using CL microscopy further revealed nanoscopic insights into these materials and their phase transformations. Based on the global features of CL spectra from the MHP films, three key spectral features (from different phases) were identified – the asymmetric broadband peak at ≈450 nm and strong peaks centered at 510 and ≈780 nm, which are respectively assigned to δ-$CsPbI_3$,[37–39] PbI_2, and band-edge emission of MHPs as shown in **Figures 2** and **3** (Figures S10 and S11, Supporting Information for mixed-halide MHPs). This allows us to map the precise spatial distribution of these phases and correlate the spatially resolved optoelectronic properties with the stoichiometric understanding provided by ToF-SIMS analysis.

We also implemented a multivariate statistical analysis – non-negative matrix factorization (NMF) – to analyze the overall CL spectra in images. This unsupervised machine learning method allows us to readily decompose the CL spectra of a scanned image into fragmental components, thereby constructing

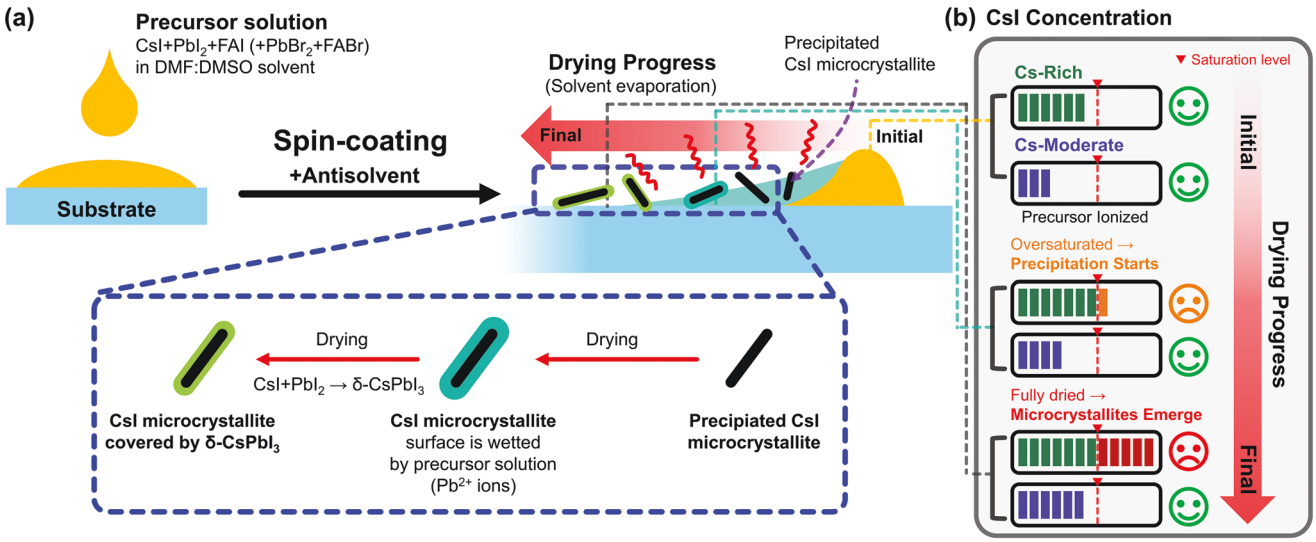

Figure 3. a) Schematic illustrating the formation pathway of CsI microcrystallites covered by δ-$CsPbI_3$ during the spin-coating process of CsFA MHP films. The right panel b) illustrates the changes in relative CsI concentration in each precursor solution (expressed with green and blue bars for Cs-rich and Cs-moderate systems, respectively) by solvent evaporation during spin-coating. At the initial stage where the concentrations are below the saturation point, the precursors are dissolved in both cases. Upon spin-coating, the solvent evaporates and CsI starts to precipitate when the concentration exceeds a saturation point (marked with a red triangle and dotted line). At the final stage where the solvent is fully dried, the microcrystallites emerge in the film, preventing the formation of homogenous α-CsFA MHP.

a spatially resolved CL map corresponding to each spectral component. As a result, each CL spectral component produced by NMF decomposition is statistically generalized, and the corresponding CL maps clearly represent the spatial distribution of the component. Through a visual inspection, depending on the complexity of CL spectra in each image, we selected the 4 to 6 components for NMF decomposition (Figures S12—S15, Supporting Information). For all CL images explored in this study, the NMF decompositions are qualitatively similar to the wavelength-specific maps that we manually selected.

Figure 2 shows scanning electron microscopy (SEM) images (Figure 2a–d), corresponding wavelength-specific CL maps (Figure 2e–h) and site-specific local CL spectra (Figure 2i–l) of Cs-rich iodide MHPs annealed at different temperatures. From the SEM image of the MHP before annealing, it was observed that rod-shaped features with diameters of around 150–200 nm intercalated within the relatively flat film matrix. These features are spatially correlated with CL signals in the 443 nm wavelength-filtered map, indicating the presence of the δ-$CsPbI_3$ phase,[40] consistent with the CsI-based aggregates observed from ToF-SIMS analysis (Figure 1a). CsI micro-crystallites could react with PbI_2 precursors, forming a δ-$CsPbI_3$ phase that covers the CsI surface (vide infra). However, at this stage, it is difficult to resolve CsI phases with CL microscopy because the 5.5 eV CsI bandgap is outside our detection window. Note that the similarity between the 443 and 512 nm bandpass-filtered CL maps is due to the broadband δ-$CsPbI_3$ CL emission and the absence of substantial PbI_2 CL in this film; the spectral overlap results in the replica of the 443 nm CL map in the 512 nm map, while the spatially localized emergence of PbI_2 produces brighter spots in the map. The CL emission of the MHP grain exhibits a strong peak centered at ≈803 nm and a relatively weak peak centered at ≈740 nm (Figure 2i). This asymmetric CL spectrum could be the sum of FA- and Cs-based α-MHP emission, respectively, suggesting the imperfect mixing of FA and Cs in the MHP.[40]

After annealing the MHP at 150 °C, flat and ribbon-like structures emitting CL characteristic of δ-$CsPbI_3$ emerge across the surface of α-MHP (Figure 2b–f,j). Meanwhile, sharp needle-like structures with a diameter of <100 nm (marked with red lines) appear on top of the ribbon structures. These structures exhibit no appreciable CL emission in our detection band of 350–1000 nm, and thus we assume they are composed of CsI. Note that the stronger CL emission from the α-MHP is observed at the grain boundaries rather than the grain surface, possibly as a result of a higher concentration of free carriers at these regions promoting radiative recombination.[41,42] Again, the similarity in 443- and 512 nm-passed CL maps is due to the broadband δ-$CsPbI_3$ CL emission and the sparsity of PbI_2 CL. For the film annealed at 200 °C, the δ-phase CL is diminished, but the PbI_2 phase centered at 510 nm starts to emerge (Figure 2c,g,k). Further raising the annealing temperature to 250 °C results in a deformation of the α-phase and the emergence of coarse crystallites on the surface of the MHP that are morphologically dissimilar from the typical MHP grain structure in the SEM image (Figure 2d). The 443 nm-filtered CL map (δ-$CsPbI_3$ emission) shows strong signals at the MHP surface and the coarse crystallites, whereas the strong 512 nm-filtered CL signals (PbI_2 emission) appear at the regions corresponding with the coarse crystallites (Figure 2h,l). This indicates that annealing at 250 °C manifests the emergence of both δ-$CsPbI_3$ and PbI_2 phases as a result of the deformation of α-MHP. Additionally, there are non-emissive CL-inactive crystallites embedded into the α-MHP matrix (highlighted with red lines) that are likely CsI as speculated above. Note that, the α-MHP phase is observed in the 766 nm-filtered CL map at the

edge of the coarse crystallites, whereas the 512 nm-filtered CL signal is positioned around the center of the coarse crystallites. This is due to the evaporation of FA by thermal decomposition as speculated in the ToF-SIMS analysis (Figure S6, Supporting Information); it is likely that the evaporation starts from the surface of the MHP grain, as schematically described in Figure S16, Supporting Information. Local CL spectra collected at several points in the scanned area (marked as *x* in both SEM image and CL maps) further reveal several other CL bands above the bandgap of MHP, possibly from the cation-segregated $CsPbI_3$ and/or δ-$FAPbI_3$.[39,40] Furthermore, it was observed that the CL emission from α-MHP phases blueshift with increasing annealing temperature due to the loss of FA cations from α-MHP (and subsequent lattice deformation) by evaporation.

If the concentration of inorganic CsI is moderate, it can be fully dissolved and ionized in solution. Then, the dissolved CsI can be homogenized with PbI_2 precursor and fully contribute to the formation of MHP with the aid of thermal annealing; indeed we observe a chemically homogeneous surface in Cs-moderate MHP system (vide infra; **Figure 4**). However, if the CsI concentration is high, CsI microcrystallites can be precipitated from the oversaturated solution during the spin-coating process. Still, these CsI microcrystallites are covered (wetted) by the precursor solution that also contains the ionized PbI_2. Complete drying of the solution leaves a structure where the surface of CsI microcrystallite is coated with PbI_2. This subsequently leads to a chemical reaction between each inorganic species at the CsI/PbI_2 interface, resulting in a thermodynamically stable δ-$CsPbI_3$ phase covering the CsI surface as illustrated in Figure 3. These cannot be fully converted to α-MHP phase unless by sufficient annealing > 320 °C;[43] however, at this temperature, decomposition of FA takes place, resulting in deformed MHP film as observed by ToF-SIMS and CL analysis (Figures S6 and S16, Supporting Information). As a consequence, once these crystallites emerge, they cannot be transformed to α-CsFA MHP during film processing.

Different spectral and morphological features were observed from the Cs-moderate iodide MHPs. Before annealing, the number of CsI micro-crystallites covered by δ-$CsPbI_3$ (i.e., rod-shaped structure; marked with yellow line) and the region emitting δ-$CsPbI_3$ CL is largely reduced (Figure 4a–e) compared with the Cs-rich iodide MHPs. In addition, the α-MHP CL exhibits a symmetric single peak, implying that the Cs^+ and FA^+ are homogeneously mixed with each other across the film (Figure 4i).

After annealing the film at 150 °C (Figure 4b,f), the residual region emitting δ-$CsPbI_3$ CL disappears, and the α-CsFA MHP CL is bright and relatively uniformly distributed across the film. Nominal grain sizes of 200–300 nm (estimated from the SEM image) are observed in the MHP with higher intensity

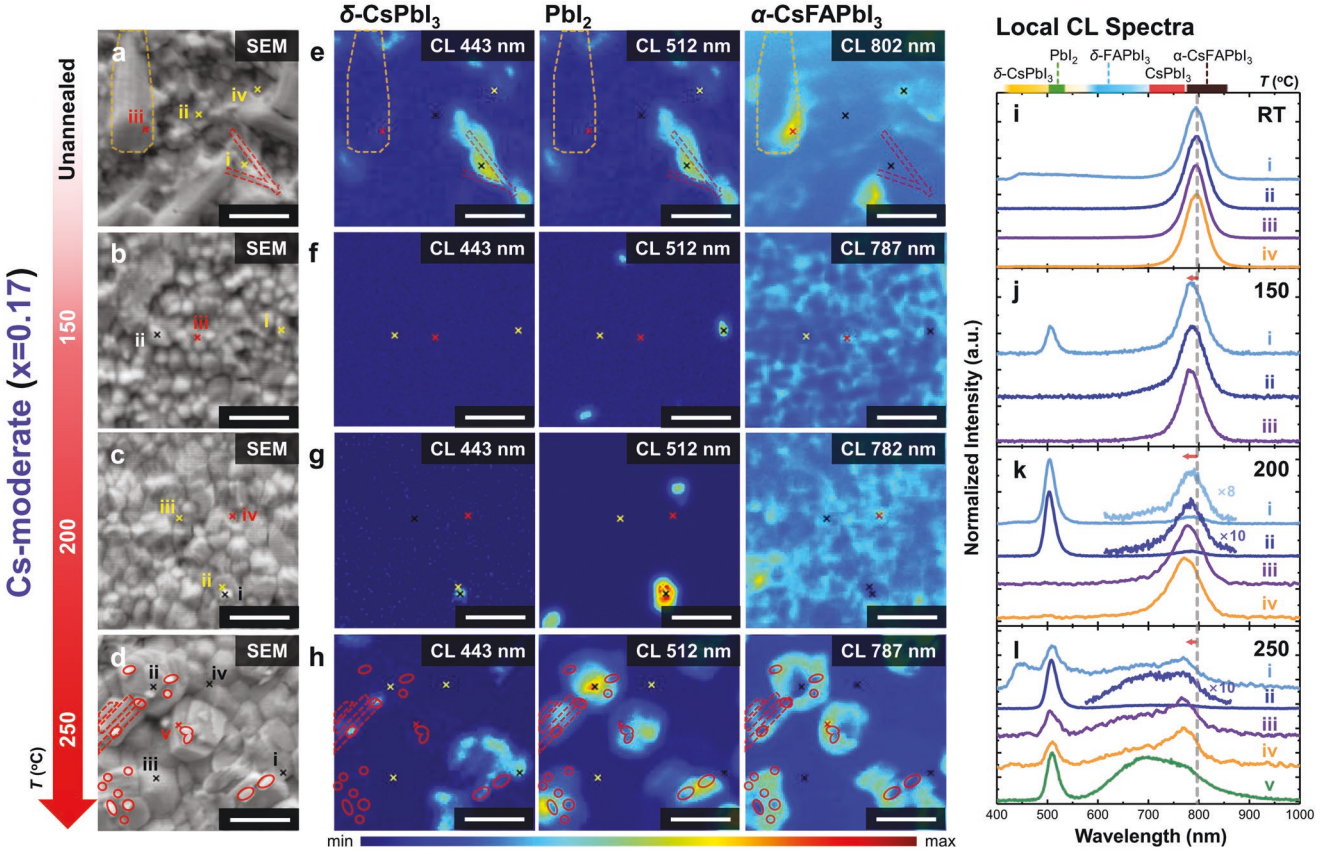

Figure 4. a–d) SEM images, e–h) CL microscopy maps, and i–l) local CL spectra (marked in SEM image) of Cs-moderate iodide MHPs, with increasing annealing temperature: a,e,i) unannealed, b,f,j) 150 °C, c,g,k) 200 °C, and d,h,l) 250 °C, respectively. Scale bar: 1 µm. The regions highlighted with red lines indicate Cs-inactive areas, assigned to be CsI. For i–l), the spectral regions where the CL peak corresponds to each phase are displayed as a color bar on top of the plot.

CL signals at the grain boundaries but no change in the spectral line shape across the film (Figure 4j). Meanwhile, PbI_2 CL emission is observed from a few isolated spots in the film. Considering the observations from that of Cs-rich MHP, these features not only suggest that 1) an appropriate Cs composition ratio is a key factor for homogeneous α-CsFA MHP growth, but also 2) the formation of the PbI_2 phase, at least at an annealing temperature of 150 °C, can be somewhat reduced once the initial CsI and δ-$CsPbI_3$ phases are consumed. Note that the Cs-moderate CsFA MHP film has demonstrated the best PV performances,[31] possibly as a result of the low density of secondary phases in this film as shown by our CL analysis.

We further explored local phase inhomogeneities in MHP films at a fixed annealing temperature of 150 °C as a function of annealing time (Figure S17, Supporting Information). For the Cs-rich MHPs, the needle-like structures emerging with prominent δ-$CsPbI_3$ (444 nm) CL bands are still intercalated in the α-CsFA MHP film matrix even after annealing for 60 min. Also, small granules exhibiting PbI_2 CL (512 nm) are also observed. These results obviously indicate that longer annealing times fail to fully convert the existing secondary phases to α-CsFA MHP. This situation is thermodynamically acceptable, as the δ-$CsPbI_3$ is known to be transformed to α-phase at annealing temperatures exceeding 320 °C.[43] In stark contrast, we could not observe such needle-like structures and the δ-$CsPbI_3$ CL from the Cs-moderate MHP after annealing for 60 min and the α-CsFA MHP film remained intact. We also explored the CL characteristics of the CsFA MHP with a smaller concentration of Cs^+ (9%) as shown in Figure S18, Supporting Information, and again, there was no appreciable CL from δ-$CsPbI_3$ and PbI_2 phases. Instead, shouldered α-CsFA MHP CL at 600–700 nm is observed. This might be attributed to the emergence of δ-$FAPbI_3$, but a more detailed investigation of MHP films with low Cs concentration would be necessary. Overall, these observations suggest that the presence of the needle-like structure and the associated chemical inhomogeneity in the MHP film is determined by the concentration of CsI in the precursor solution and cannot be mediated by annealing conditions.

There is a nontrivial discrepancy in the CL peak position of α-MHP between the grain and grain-boundary regions for the Cs-rich MHP annealed at 150 °C; CL peaks from the boundaries are blueshifted by ≈16 nm (32 meV) compared with the CL within grains (Figure S19a,b, Supporting Information). This difference can be explained by the compositional inhomogeneity of the cations: the Cs-enriched composition of the MHP at the grain boundaries[44] results in a larger band gap with an upshifted conduction band minimum.[45,46] However, we didn't observe these features in the Cs-moderate MHP (Figure S19c and S19d). This suggests that excessive Cs also result in local inhomogeneity of the α-MHP phase composition.

When increasing the annealing temperature to 200 °C (Figure 4c,g,k), the density of the PbI_2 phase increased and the δ-phase appeared in the Cs-moderate iodide MHP. Analogous to the Cs-rich system, annealing of the film at 250 °C resulted in the pronounced appearance of δ-phases, CsI, and PbI_2 and a broadband CL band centered at ≈710 nm that indicates complex deformation of α-CsFA MHP to δ-phases (Figure 4d,h,l).[40] Also, the CL of the α-MHP blueshifted with increasing temperature. Again, these observations suggest that excessively high temperatures cause losses of FA by evaporation, as speculated from ToF-SIMS measurements (Figure S7, Supporting Information), resulting in chemical complexities in the MHP film and degradation of the optoelectronic properties.

Together, CL analysis reveals that the CsI-based aggregates (observed from ToF-SIMS; Figure 1a) in the MHPs before annealing are CsI micro-crystallites covered by δ-$CsPbI_3$. In Cs-moderate MHPs, these aggregates are fully transformed to a homogeneous α-CsFA MHP phase by annealing at 150 °C, while in Cs-rich MHP, some of the aggregates remain even after annealing for longer times or at higher temperatures. In addition, Cs-rich MHPs exhibit a larger bandgap at grain boundaries compared to within the grains, while the Cs-moderate MHP exhibits a more homogeneous bandgap across the film. Annealing at higher temperatures (≈250 °C) deforms the α-CsFA MHPs via thermal decomposition, subsequently leaving PbI_2 and δ-phases in the films.

It should be noted that classical global characterization techniques like X-ray diffraction (XRD) analysis only provide limited insight into chemical inhomogeneities associated with the MHP films. We collected XRD patterns of the MHPs before annealing (Figure S20, Supporting Information), revealing the coexistence of substantial δ-phase and α-CsFA MHP phase. However, due to the strong peak overlap between CsI (110) and α-CsFA MHP (200) at $2\theta = \approx 27.5°$, as well as the small CsI crystallites compared to the surrounding δ-$CsPbI_3$ phase, it is impossible to claim the existence of CsI via XRD analysis.

We observe that the local phase inhomogeneities are largely mediated in mixed-halide MHPs, suggesting that the Br incorporation promotes homogenization of A-site cations in the CsFA MHP systems (Note S2, Figures S10,S11, and S21—S23, Supporting Information).

To explore the effect of inhomogeneity and secondary phases on (photo-)carrier transport in CsFA MHPs, conductive atomic force microscopy (cAFM) measurements were performed under light/dark conditions. For each composition, we compared the local conductivity of the films annealed at 150 and 250 °C. This allows us to identify the influence of secondary phases on the local conductivity of the systems. For Cs-rich iodide MHPs, the cAFM image of the film prepared at 150 °C exhibited high levels of local current. However, there was a region where the current flow was blocked that is likely covered with δ-$CsPbI_3$ as revealed by CL analysis (**Figure 5**a). Upon light irradiation, the current notably increases due to photogenerated carriers but the current flow through the area covered with the secondary phase is still nearly forbidden (Figure 5b). Such a current-blocking feature is more pronounced in the film annealed at 250 °C (Figure 5c) because of the prominence of secondary phases (in this case, PbI_2 rather than δ-$CsPbI_3$). Interestingly, we observe that the local dark current and the photocurrent are substantially suppressed (Figure 5d). However, for the Cs-moderate iodide MHPs, the film annealed at 150 °C exhibited high levels of dark current and photocurrent and negligible density of current blocked regions (Figure 5e,f). This is consistent with the CL results, where the α-CsFA MHP surface is almost free from secondary phases. After annealing the film at 250 °C, considerable current-blocked areas emerge, and the local dark current and photocurrent are suppressed (Figure 5g,h).

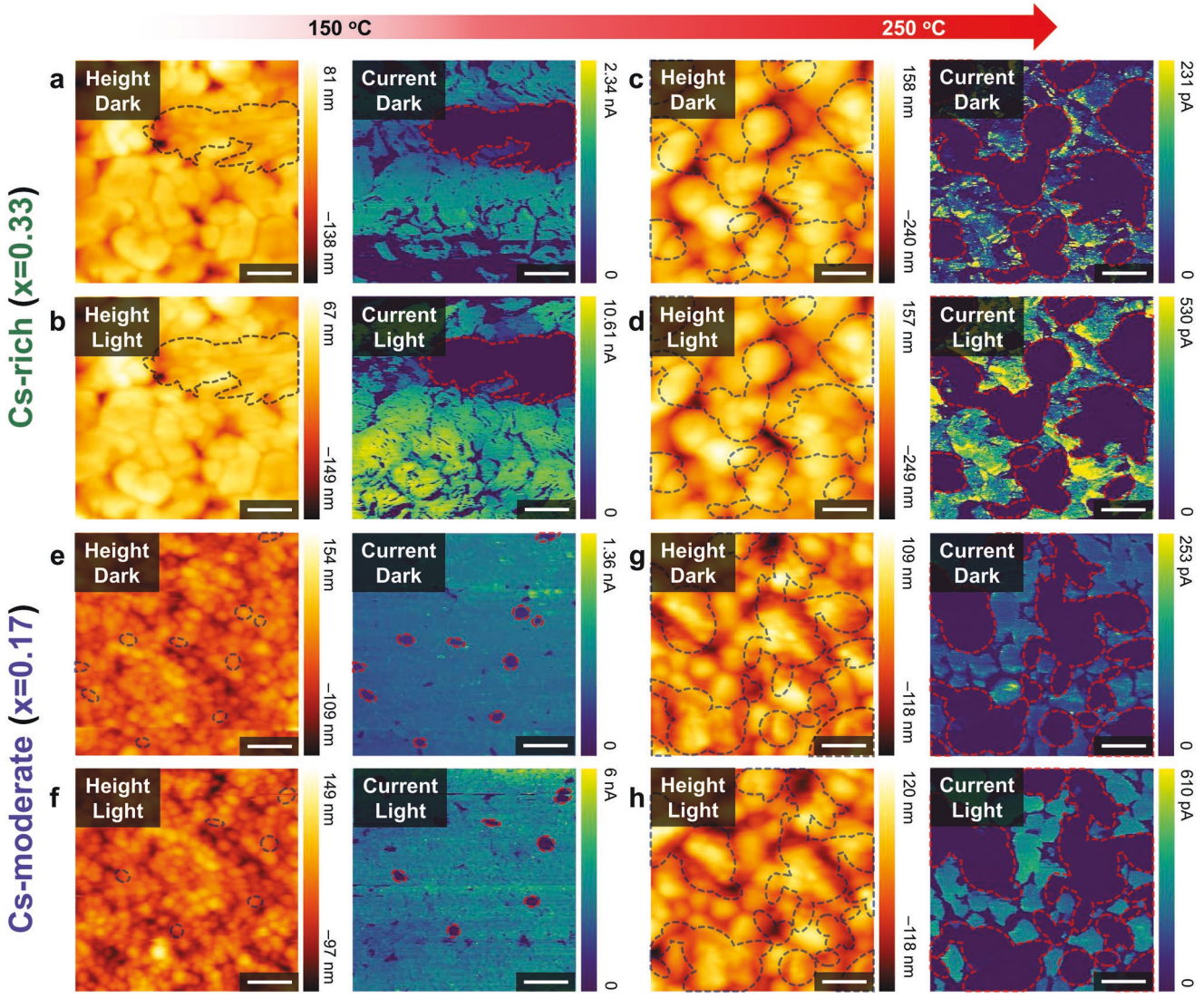

Figure 5. cAFM height (left) and current profiles (right) of a–d) Cs-rich and e–h) Cs-moderate iodide MHPs prepared at different annealing temperatures: a,b,e,f) 150 °C and c,d,g,h) 250 °C. For each MHP film, the current profiles under a,c,e,g) dark and b,d,f,h) light conditions were measured at the same spot, respectively. Scale bar: 1 µm. The low-current flowing regions are respectively marked with black and red lines in height and current maps.

Though we could not reasonably separate the contribution of ionic transport from the total current, these observations clearly suggest that the secondary phases spatially covering the α-CsFA MHP matrix totally inhibit current flow across the film. The excessive annealing temperature can degrade the α-CsFA MHP by introducing uncontrolled local inhomogeneities in the matrix and reducing the density of the photoactive phase. This is consistent with the parasitic CL bands (e.g., $CsPbI_3$ and/or δ-$FAPbI_3$ phase-segregated) at the grain surfaces.

The mixed-halide CsFA MHPs exhibit similar features to the iodide MHPs (Figure S24, Supporting Information). However, a lower dark current is typically observed at the grain boundaries for the samples annealed at 150 °C. Such a local difference could be explained by a Br-rich composition at the grain boundaries as previously reported, which suppresses the local dark current.[47] Under light irradiation, the Cs-moderate MHP exhibits increased local photocurrent at grain boundaries as a result of charge funneling towards these regions.[48] However, despite this local increase in photocurrent, the suppression of current flow at the grain boundaries is pronounced in the Cs-rich MHPs. This is due to suppressed halide segregation (particularly, iodine-rich grain boundaries) by larger amounts of Cs in MHP as previously observed.[49] After annealing the films at 250 °C, the local current in the areas without secondary phases on the surface is drastically suppressed. Significant phase inhomogeneities created in these films, observed from CL analysis, may substantially impede charge transport through the films and produce fewer photocarriers.

Kelvin probe force microscopy (KPFM) analysis further reveals the electronic structure of the MHP systems, provides complementary insights into the nanoscopic chemical inhomogeneities of the α-CsFA MHP matrix and reveals energy-level distortion by defective secondary phases. For the Cs-rich iodide MHP annealed at 150 °C, several spots on the surface

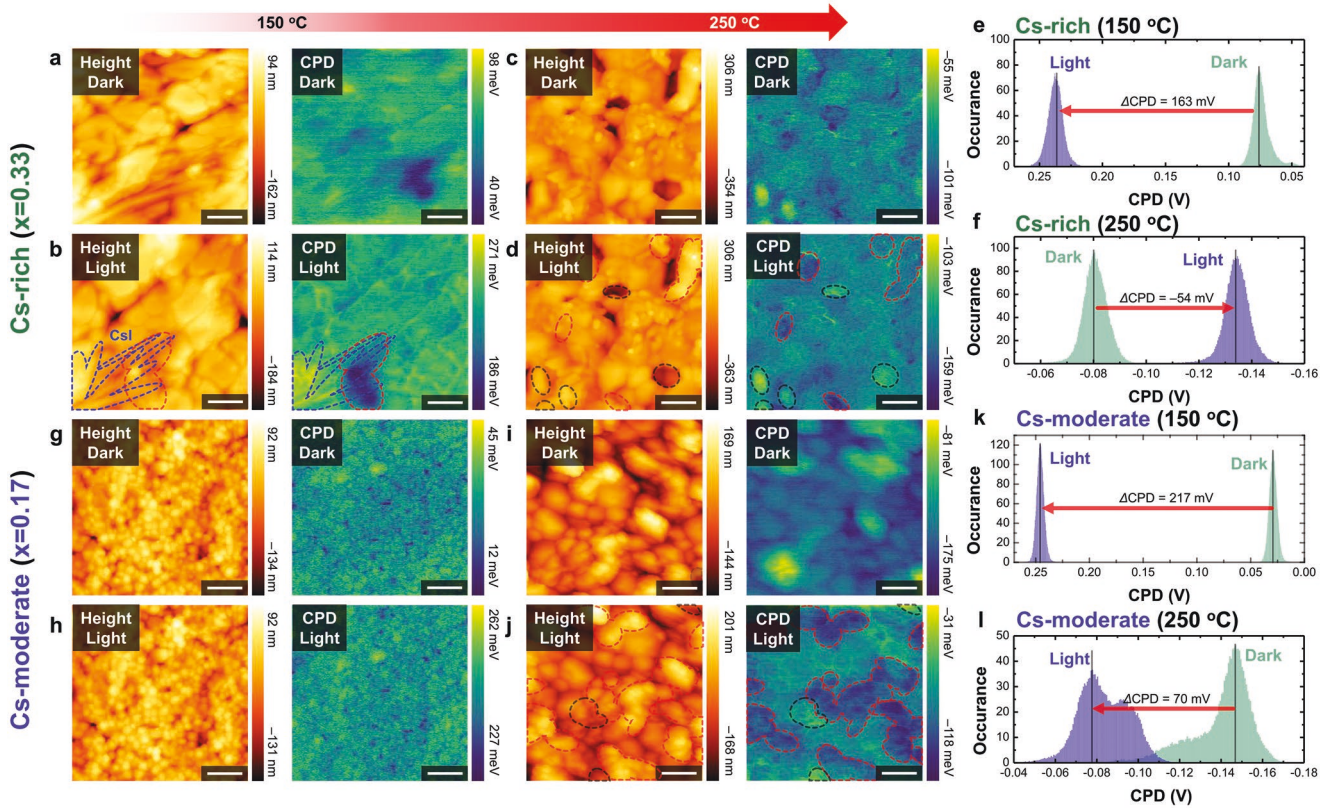

Figure 6. KPFM height (left) and CPD profiles (right) of a–d) Cs-rich and g–j) Cs-moderate iodide MHPs prepared at different annealing temperatures: a,b,g,h) 150 °C and c,d,i,j) 250 °C. For each MHP film, the current profiles under a,c,g,i) dark and b,d,h,j) light were measured at the same spot, respectively. Scale bar: 1 µm. e,f,k,l) CPD distributions of the corresponding MHP films. The low and high CPD regions are respectively marked with red and black lines.

(red-marked) that are likely to be the secondary phases exhibited lower contact potential difference (CPD) – a difference of work function between the AFM tip and surface – than that of the MHP grain (**Figure 6**a). This indicates the secondary phases exhibit lower work functions than MHP, distorting the local electronic structures. Under light irradiation, the level of CPD over the surface is increased by 163 mV, which corresponds to the surface photovoltage of the α-CsFA MHP (Figure 6b–e). Meanwhile, the local CPD inhomogeneities, mainly identified at the grain boundaries and secondary phases, become more pronounced under light irradiation, contributing to the larger CPD distribution width. We observe higher CPD at grain boundaries of the MHP film than in grains when the sample is optically excited but no appreciable differences under dark conditions, which could be a result of photogenerated hole accumulation in the shallower valence band associated with these regions.[44,50,51] It should be noted that this MHP contains only iodide, and therefore halide segregation is not responsible for the CPD inhomogeneity. A Cs-enriched cation composition formed at the grain boundaries – observed from CL analysis (Figure S19, Supporting Information) – would explain this heterogeneity, and would also be consistent with previous reports.[44,45] A type-II heterojunction near grain boundaries associated with this compositional heterogeneity can block electrons and allow hole accumulation. The secondary phases exhibit distinctive local CPD drops, but there are some regions – around the sharp needle-like structures that are likely CsI – showing an increase in CPD (highlighted with a blue-dashed line). Given the shallow work function of CsI,[52] the increased CPD at these regions could be attributed to hole accumulation in CsI. The lower CPD regions covering a broad area could be assigned to δ-phases based on our CL phase identification. Notably depressed CPD distributions are observed after annealing the sample at 250 °C, although the hole accumulation at the grain boundary becomes weaker (Figure 6c). Light irradiation further suppresses the average CPD level and upshifts the work function by 54 mV (Figure 6d,f). While further in-depth investigations of this feature are necessary, the unfavorable secondary-phase energy levels (i.e., δ-phase and PbI_2) may severely dissipate photogenerated charges from the α-MHP, thereby resulting in the negative shift in CPD level.[53]

By contrast, after annealing at 150 °C, the Cs-moderate MHP exhibits a homogeneous CPD distribution over the grain and slightly lower CPD at the grain boundaries, consistent with previous observations (Figure 6g).[44] Also, under light irradiation, the CPD level increases and results in a surface photovoltage (i.e., CPD difference between the light and dark condition) of 217 meV, but the change of local contrast in CPD is negligible (Figure 6h–k). This similar CPD contrast under dark and light conditions could be attributed to the high conductivity of a film that is free from structural inhomogeneity, as confirmed by the cAFM analysis. Such a homogeneous film exhibits optimized

photocurrent and photovoltage with minimal carrier loss and is thus ideal for PV applications. This observed homogeneity can also explain the exceptional performances of CsFA MHP PVs employing the same Cs composition ratio.[21,31] After annealing at 250 °C, it is again observed that local CPDs at the secondary phases are lower than those of the underlying MHP grains (Figure 6i). Under light irradiation, a smaller CPD increase (70 mV) is observed, and the CPD at grain boundaries increases (Figure 6j,l). This indicates that, even for the homogenized MHP with an optimal Cs composition ratio, annealing at excessive temperatures impedes the phase homogeneity, creating off-stoichiometric MHP lattices with local structural discrepancies. Meanwhile, lower CPDs at the secondary phases in this film are observed, potentially due to the dissipation of photocarriers by these defective structures (Figure S25, Supporting Information).

The same local CPD trends are observed on both mixed-halide films (Figure S26, Supporting Information). Note that, regardless of the halide composition, a common feature is observed. The Cs-rich MHP annealed at 250 °C exhibits a lower CPD level under light compared to the CPD measured under dark conditions (Figure 6f and Figure S26f, Supporting Information). Though the exact reason for this trend is elusive, it could be explained by Cs-rich metallic states on the MHP surface that results in shallow work functions and thereby reduced CPDs under light irradiation.

Collectively, both cAFM and KPFM results reveal that secondary phases significantly compromise the optoelectronic properties of the MHPs. cAFM analysis confirms that the secondary phases are insulators that suppress the conductivity and photocurrent in the MHPs. The secondary phases could be attributed to CsI micro-crystallites or thermal decomposition of the MHPs as observed from CL analysis. KPFM analysis shows the largely different energy level structures of the secondary phases with α-CsFA MHP phase, resulting in inhomogeneous surface potential. In device integration, this not only causes inefficient charge transfer to neighboring charge transport layers but also severely compromises the photovoltage. These observations suggest that neither the control of annealing temperature nor the annealing time are sufficient to achieve a functional phase-pure α-CsFA MHP. Appropriate choices of solvents and additives could be effective ways to synthesize phase-pure structures in Cs-rich MHPs.

3. Outlook

In summary, we comprehensively explored the chemical complexity and the consequent charge transport behaviors and electronic structures in CsFA MHP systems with complementary microscopies. Spatially resolved ToF-SIMS and hyperspectral CL microscopy clearly identify the nontrivial macro- and microscopic local chemical inhomogeneities in the functional MHP matrices and capture the chemical actions associated with the structural evolution. As a result, these microscopy analyses allow us to draw a complete chemical landscape associated with the fate of the local inhomogeneities in the MHP systems, which are known to play crucial roles in the performance and longevity of PV devices. We revealed that substantial chemical inhomogeneities – with considerable quantities of CsI and δ-$CsPbI_3$ phases – are present in Cs-rich MHPs at the beginning stage of crystallization, and these inhomogeneities cannot be fully converted to a photoactive α-CsFA MHP phase by annealing. Reducing the Cs compositional ratio can mediate the formation of undesired phases after solution processing, and appropriate thermal annealing further homogenizes the film to be nearly free from phase inhomogeneities. Meanwhile, thermal annealing also initiates the formation of PbI_2 phases, and other defective phases emerge in the MHPs with increasing annealing temperature. Excessive Cs also result in Cs-enriched grain boundaries and a more disordered energy-level landscape. The incorporation of Br further regulates the local inhomogeneities at the initial stage, and cAFM and KPFM analysis reveal that such defective inhomogeneities compromise the optoelectronic properties of MHP films, particularly the conductivity, photocurrent, and photovoltages. All these observations suggest that the practical aspects associated with the film fabrication stage – beyond the typical Goldschmidt tolerance factor or thermodynamic predictions based on calculations –must be further considered for the synthesis of CsFA MHPs. Note that this argument can also be generalized to other MHP systems, such as $FAPbI_3$, where a variety of chemical additives need to be included for the film fabrication. This can also cause local chemical complexities in the matrices. The key observations and fundamentals uncovered in this study provide a blueprint for the design of materials and devices with an emphasis on controlling the MHP's optoelectronic properties.

4. Experimental Section

Fabrication of MHP Films: First, 1.2 M of four different $Cs_xFA_{1-x}Pb(Br_yI_{1-y})_3$ MHP precursor solutions (x = 0.17 and 0.33, and y = 0 and 0.17) were prepared by dissolving a mixture of respective amounts of PbI_2, FAI, $PbBr_2$ and CsI in a mixed solvent of DMF and DMSO (DMF (v):DMSO (v) = 2:1) in an N_2 glovebox (< 2 ppm of O_2 and H_2O). These solutions were respectively spin-coated on the FTO substrates. A two-step spin-coating process was used for making the films; 1000 rpm 10 s(1000 rpm s^{-1}) followed by 6000 rpm 20 s (2000 rpm s^{-1}), with the MHP solution added before spin-coating. Chlorobenzene was gently added 5 s before the end of the second step. The films were then annealed at the target temperature (i.e., 150, 200, and 250 °C) for 10 min. Films were transported in vacuum-sealed containers.

ToF-SIMS Measurements: ToF-SIMS measurements were performed using the ToF-SIMS.5.NSC instrument (ION.TOF GmbH, Germany) with a vacuum level at the main chamber of around 10^{-8} mbar. Bi_3^{++} ion gun with the energy of 30 keV, DC current ≈0.5 nA, and spot sizer ≈120 nm was used as the primary ion source for chemical analysis. Experiments were carried out in positive and negative ion detection modes with mass resolution m/Dm = 100–500. Low energy electron flood gun was used for charge compensation during the experiments.

Hyperspectral CL Microscopy: An FEI Quattro environmental SEM with a Delmic Sparc CL collection module, utilizing a parabolic mirror to collect the CL signals from the film upon e-beam excitation, was used. An electron beam with an acceleration voltage of 5 kV (with a beam current of 32 pA) was passed through a hole in the parabolic mirror for sample excitation and an acquisition time of 400 ms per spectrum was used for CL signal collection. The pixel size was set to 40 nm. All measurements were conducted in a low vacuum environment of 50 Pa H_2O vapor to effectively mitigate sample charging. It was noted that such measurement conditions did not cause any observable sample degradation during measurement (over a week).

XRD Characterization: XRD patterns of the MHP films before annealing were collected by using a high-resolution X-ray diffractometer (Empyrean, Malvern Panalytical).

Non-Negative Matrix Factorization (NMF) Analysis: NMF was a classical form of the unsupervised unmixing machine learning approach. This was an algorithm in multivariate analysis. An input data was factorized into desired endmember-abundance pairs with the property that all endmembers had no negative components. Particularly, this approach was suitable for analyzing CL data where all spectra in a spatial map were inherently non-negative due to calculating molecular mass. NMF data analysis was performed on google Colab using Python 3.6 and scikit-learn 0.22.1 library.

cAFM and KPFM Measurements: A commercial AFM (Cypher, Oxford Instrument) was used for the measurements with a Pt/Ir-coated Si AFM tip (ElectriMulti 75G, Budget Sensors). For cAFM, a dual-gain ORCA (Oxford Instrument) cantilever holder was used. A conductive wire was soldered on the metal sample holder. This was mounted into the instrument to establish a closed electric circuit between the tip and sample and a fixed bias of 2 V was applied to the film. For KPFM, a lift height of 40 nm was used to detect the optimized CPD. The light irradiation and dark condition were established by modulating the aperture size of the microscope light source from 100 to 0%.

Supporting Information

Supporting Information is available from the Wiley Online Library or from the author.

Acknowledgements

J.Y. and M.A. acknowledge support from National Science Foundation (NSF), Award Number No. 2043205. All authors acknowledge support from the Center for Nanophase Materials Sciences (CNMS) user facility, projects CNMS2022-A-01171 and CNMS2022-A-01219. Scanning probe, ToF-SIMS, and cathodoluminescence microscopy were performed at the CNMS, which is a U.S. Department of Energy Office of Science User Facility. D.K.L. was funded by a National Science Foundation Graduate Research Fellowship Program under Grant No. DGE-2039655. J.P.C.B. is partly funded by the Goizueta Foundation and the Micron Foundation. Any opinions, findings, and conclusions or recommendations expressed in this material are those of the author(s) and do not necessarily reflect the views of the National Science Foundation.

Conflict of Interest

The authors declare no conflict of interest.

Data Availability Statement

The data that support the findings of this study are available from the corresponding author upon reasonable request.

Keywords

cathodoluminescence, cesium ratio, halide perovskites, inhomogeneity, methylammonium free

Received: August 23, 2022
Revised: November 23, 2022
Published online:

[1] A. Al-Ashouri, E. Kohnen, B. Li, A. Magomedov, H. Hempel, P. Caprioglio, J. A. Marquez, A. B. M. Vilches, E. Kasparavicius, J. A. Smith, N. Phung, D. Menzel, M. Grischek, L. Kegelmann, D. Skroblin, C. Gollwitzer, T. Malinauskas, M. Jost, G. Matic, B. Rech, R. Schlatmann, M. Topic, L. Korte, A. Abate, B. Stannowski, D. Neher, M. Stolterfoht, T. Unold, V. Getautis, S. Albrecht, *Science* **2020**, *370*, 1300.
[2] J. Jeong, M. Kim, J. Seo, H. Lu, P. Ahlawat, A. Mishra, Y. Yang, M. A. Hope, F. T. Eickemeyer, M. Kim, Y. J. Yoon, I. W. Choi, B. P. Darwich, S. J. Choi, Y. Jo, J. H. Lee, B. Walker, S. M. Zakeeruddin, L. Emsley, U. Rothlisberger, A. Hagfeldt, D. S. Kim, M. Gratzel, J. Y. Kim, *Nature* **2021**, *592*, 381.
[3] H. Min, D. Y. Lee, J. Kim, G. Kim, K. S. Lee, J. Kim, M. J. Paik, Y. K. Kim, K. S. Kim, M. G. Kim, T. J. Shin, S. Il Seok, *Nature* **2021**, *598*, 444.
[4] J. J. Yoo, G. Seo, M. R. Chua, T. G. Park, Y. Lu, F. Rotermund, Y. K. Kim, C. S. Moon, N. J. Jeon, J. P. Correa-Baena, V. Bulovic, S. S. Shin, M. G. Bawendi, J. Seo, *Nature* **2021**, *590*, 587.
[5] NREL, Best Research-Cell Efficiency Chart **2022**.
[6] T. Chen, B. J. Foley, C. Park, C. M. Brown, L. W. Harriger, J. Lee, J. Ruff, M. Yoon, J. J. Choi, S. H. Lee, *Sci. Adv.* **2016**, *2*, 1601650.
[7] F. Cordero, F. Craciun, F. Trequattrini, A. Generosi, B. Paci, A. M. Paoletti, G. Pennesi, *J. Phys. Chem. Lett.* **2019**, *10*, 2463.
[8] M. Saliba, T. Matsui, K. Domanski, J. Y. Seo, A. Ummadisingu, S. M. Zakeeruddin, J. P. Correa-Baena, W. R. Tress, A. Abate, A. Hagfeldt, M. Gratzel, *Science* **2016**, *354*, 206.
[9] M. Saliba, T. Matsui, J. Y. Seo, K. Domanski, J. P. Correa-Baena, M. K. Nazeeruddin, S. M. Zakeeruddin, W. Tress, A. Abate, A. Hagfeldt, M. Gratzel, *Energy Environ. Sci.* **2016**, *9*, 1989.
[10] S. Wang, A. Wang, F. Hao, *iScience* **2022**, *25*, 103599.
[11] C. Yi, J. Luo, S. Meloni, A. Boziki, N. Ashari-Astani, C. Gratzel, S. M. Zakeeruddin, U. Rothlisberger, M. Gratzel, *Energy Environ. Sci.* **2016**, *9*, 656.
[12] P. Caprioglio, S. Caicedo-Davila, T. C. J. Yang, C. M. Wolff, F. Pena-Camargo, P. Fiala, B. Rech, C. Ballif, D. Abou-Ras, M. Stolterfoht, S. Albrecht, Q. Jeangros, D. Neher, *ACS Energy Lett.* **2021**, *6*, 419.
[13] K. Frohna, M. Anaya, S. Macpherson, J. Sung, T. A. S. Doherty, Y. H. Chiang, A. J. Winchester, K. W. P. Orr, J. E. Parker, P. D. Quinn, K. M. Dani, A. Rao, S. D. Stranks, *Nat. Nanotechnol.* **2022**, *17*, 190.
[14] Y. An, J. Hidalgo, C. A. R. Perini, A. F. Castro-Mendez, J. N. Vagott, K. Bairley, S. Wang, X. Li, J. P. Correa-Baena, *ACS Energy Lett.* **2021**, *6*, 1942.
[15] A. Boziki, D. J. Kubicki, A. Mishra, S. Meloni, L. Emsley, M. Gratzel, U. Rothlisberger, *Chem. Mater.* **2020**, *32*, 2605.
[16] Z. Li, M. Yang, J. S. Park, S. H. Wei, J. J. Berry, K. Zhu, *Chem. Mater.* **2016**, *28*, 284.
[17] X. X. Gao, W. Luo, Y. Zhang, R. Hu, B. Zhang, A. Zuttel, Y. Feng, M. K. Nazeeruddin, *Adv. Mater.* **2020**, *32*, 1905502.
[18] S. Gharibzadeh, P. Fassi, I. M. Hossain, P. Rohrbeck, M. Frericks, M. Schmidt, T. Duong, M. R. Khan, T. Abzieher, B. A. Nejand, F. Schackmar, A. Osbel, T. Feeney, R. Singh, D. Fuchs, U. Lemmer, J. P. Hofmann, S. A. L. Weber, U. W. Paetzold, *Energy Environ. Sci.* **2021**, *14*, 5875.
[19] J. P. Correa-Baena, Y. Luo, T. M. Brenner, J. Snaider, S. Sun, X. Li, M. A. Jensen, N. T. P. Hartono, L. Nienhaus, S. Wieghold, J. R. Poindexter, S. Wang, Y. S. Meng, T. Wang, B. Lai, M. V. Holt, Z. Cai, M. G. Bawendi, L. Huang, T. Buonassisi, D. P. Fenning, *Science* **2019**, *363*, 627.
[20] S. Macpherson, T. A. S. Doherty, A. J. Winchester, S. Kosar, D. N. Johnstone, Y. H. Chiang, K. Galkowski, M. Anaya, K. Frohna, A. N. Iqbal, S. Nagane, B. Roose, Z. Andaji-Garmaroudi, K. W. P. Orr, J. E. Parker, P. A. Midgley, K. M. Dani, S. D. Stranks, *Nature* **2022**, *607*, 294.

[21] T. Bu, J. Li, H. Li, C. Tian, J. Su, G. Tong, L. K. Ono, C. Wang, Z. Lin, N. Chai, X. L. Zhang, J. Chang, J. Lu, J. Zhong, W. Huang, Y. Qi, Y. B. Cheng, F. Huang, *Science* **2021**, *372*, 1327.
[22] R. Szostak, P. E. Marchezi, A. d. S. Marques, J. C. da Silva, M. S. de Holanda, M. M. Soares, H. C. N. Tolentino, A. F. Nogueira, *Sustainable Energy Fuels* **2019**, *3*, 2287.
[23] Y. Hu, M. F. Ayguler, M. L. Petrus, T. Bein, P. Docampo, *ACS Energy Lett.* **2017**, *2*, 2212.
[24] D. J. Kubicki, D. Prochowicz, A. Hofstetter, S. M. Zakeeruddin, M. Gratzel, L. Emsley, *J. Am. Chem. Soc.* **2017**, *139*, 14173.
[25] Q. An, F. Paulus, D. Becker-Koch, C. Cho, Q. Sun, A. Weu, S. Bitton, N. Tessler, Y. Vaynzof, *Matter* **2021**, *5*, 1683.
[26] S. P. Harvey, Z. Li, J. A. Christians, K. Zhu, J. M. Luther, J. J. Berry, *ACS Appl. Mater. Interfaces* **2018**, *10* ,28541.
[27] K. Higgins, M. Lorenz, M. Ziatdinov, R. K. Vasudevan, A. V. Ievlev, E. D. Lukosi, O. S. Ovchinnikova, S. V. Kalinin, M. Ahmadi, *Adv. Funct. Mater.* **2020**, *30*, 2001995.
[28] Y. Liu, A. V. Ievlev, N. Borodinov, M. Lorenz, K. Xiao, M. Ahmadi, B. Hu, S. V. Kalinin, O. S. Ovchinnikova, *Adv. Funct. Mater.* **2021**, *31*, 2008777.
[29] Y. Liu, M. Lorenz, A. V. Ievlev, O. S. Ovchinnikova, *Adv. Funct. Mater.* **2020**, *30*, 2002201.
[30] D. W. deQuilettes, S. M. Vorpahl, S. D. Stranks, H. Nagaoka, G. E. Eperon, M. E. Ziffer, H. J. Snaith, D. S. Ginger, *Science* **2015**, *348*, 683.
[31] Y. An, C. A. R. Perini, J. Hidalgo, A. F. Castro-Mendez, J. N. Vagott, R. Li, W. A. Saidi, S. Wang, X. Li, J. P. Correa-Baena, *Energy Environ. Sci.* **2021**, *14*, 6638.
[32] D. H. Choi, H. J. Seok, S. K. Kim, D. H. Kim, B. Hou, H. K. Kim, *Sol. RRL* **2021**, *5*, 2100660.
[33] K. Ho, M. Wei, E. H. Sargent, G. C. Walker, *ACS Energy Lett.* **2021**, *6*, 934.
[34] L. Ma, D. Q. Guo, M. T. Li, C. Wang, Z. L. Zhou, X. Zhao, F. T. Zhang, Z. M. Ao, Z. G. Nie, *Chem. Mater.* **2019**, *31*, 8515.
[35] L. Brewer, E. Brackett, *Chem. Rev.* **1961**, *61*, 425.
[36] J. Yang, X. Liu, Y. Zhang, X. Zheng, X. He, H. Wang, F. Yue, S. Braun, J. Chen, J. Xu, Y. Li, Y. Jin, J. Tang, C. Duan, M. Fahlman, Q. Bao, *Nano Energy* **2018**, *54*, 218.
[37] J. Chen, J. Wang, X. Xu, J. Li, J. Song, S. Lan, S. Liu, B. Cai, B. Han, J. T. Precht, D. Ginger, H. Zeng, *Nat. Photonics* **2021**, *15*, 238.
[38] M. Lai, Q. Kong, C. G. Bischak, Y. Yu, L. Dou, S. W. Eaton, N. S. Ginsberg, P. Yang, *Nano Res.* **2017**, *10*, 1107.
[39] F. Ma, J. Li, W. Li, N. Lin, L. Wang, J. Qiao, *Chem. Sci.* **2017**, *8*, 800.
[40] P. Wang, X. Chen, T. Liu, C. H. Hou, Y. Tian, X. Xu, Z. Chen, P. Ran, T. Jiang, C. H. Kuan, B. Yan, J. Yao, J. J. Shyue, J. Qiu, Y. M. Yang, *Small Methods* **2022**, *6*, 2200048.
[41] H. Guthrey, J. Moseley, *Adv. Energy Mater.* **2020**, *10*, 1903840.
[42] W. Li, M. U. Rothmann, A. Liu, Z. Wang, Y. Zhang, A. R. Pascoe, J. Lu, L. Jiang, Y. Chen, F. Huang, Y. P. , Q. Bao, J. Etheridge, U. Bach, Y. B. Cheng, *Adv. Energy Mater.* **2017**, *7*, 1700946.
[43] L. T. Schelhas, Z. Li, J. A. Christians, A. Goyal, P. Kairys, S. P. Harvey, D. H. Kim, K. H. Stone, J. M. Luther, K. Zhu, V. Stevanovic, J. J. Berry, *Energy Environ. Sci.* **2019**, *12*, 1341.
[44] Z. Peng, Q. Wei, H. Chen, Y. Liu, F. Wang, X. Jiang, W. Liu, W. Zhou, S. Ling, Z. Ning, *Cell Rep. Phys. Sci.* **2020**, *1*, 100224.
[45] N. X. Li, Y. Q. Luo, Z. H. Chen, X. X. Niu, X. Zhang, J. Z. Lu, R. Kumar, J. K. Jiang, H. F. Liu, X. Guo, B. Lai, G. Brocks, Q. Chen, S. X. Tao, D. P. Fenning, H. P. Zhou, *Joule* **2020**, *4*, 1743.
[46] S. Tao, I. Schmidt, G. Brocks, J. Jiang, I. Tranca, K. Meerholz, S. Olthof, *Nat. Commun.* **2019**, *10*, 2560.
[47] M. I. Saidaminov, K. Williams, M. Wei, A. Johnston, R. Quintero-Bermudez, M. Vafaie, J. M. Pina, A. H. Proppe, Y. Hou, G. Walters, S. O. Kelley, W. A. Tisdale, E. H. Sargent, *Nat. Mater.* **2020**, *19*, 412.
[48] H. Wu, C. Xu, Z. Zhang, Z. Xiong, M. Shi, S. Ma, W. Fan, Z. Zhang, Q. Liao, Z. Kang, Y. Zhang, *Nano Lett.* **2022**, *22*, 1467.
[49] K. A. Bush, K. Fronha, R. Prasanna, R. E. Beal, T. Leijtens, S. A. Swifter, M. D. McGehee, *ACS Energy Lett.* **2018**, *3*, 428.
[50] P. Gratia, G. Grancini, J. N. Audinot, X. Jeanbourquin, E. Mosconi, I. Zimmermann, D. Dowsett, Y. Lee, M. Gratzel, F. De Angelis, K. Sivula, T. Wirtz, M. K. Nazeeruddin, *J. Am. Chem. Soc.* **2016**, *138*, 15821.
[51] D. Toth, B. Hailegnaw, F. Richheimer, F. A. Castro, F. Kienberger, M. C. Scharber, S. Wood, G. Gramse, *ACS Appl. Mater. Interfaces* **2020**, *12*, 48057.
[52] S. B. Fairchild, T. C. Back, P. T. Murray, M. M. Cahay, D. A. Shiffler, *J. Vac. Sci. Technol., A* **2011**, *29*, 031402.
[53] T. J. Jacobsson, J. P. Correa-Baena, E. H. Anaraki, B. Philippe, S. D. Stranks, M. E. F. Bouduban, W. Tress, K. Schenk, J. Teuscher, J. E. Moser, H. Rensmo, A. Hagfeldt, *J. Am. Chem. Soc.* **2016**, *138*, 10331.